

Impact of Control Parameters on Angular Stability of Grid-Forming Converters Using Virtual-Admittance Based Control

Downloaded from: https://research.chalmers.se, 2026-11-23 00:27 UTC

Citation for the original published paper (version of record):

Kamalinejad, K., Narula, A., Bongiorno, M. et al (2025). Impact of Control Parameters on Angular Stability of Grid-Forming Converters Using
Virtual-Admittance Based Control. 2025 Energy Conversion Congress and Expo Europe Ecce Europe 2025 Proceedings. http://dx.doi.org/10.1109/ECCE-Europe62795.2025.11238912

N.B. When citing this work, cite the original published paper.

research.chalmers.se offers the possibility of retrieving research publications produced at Chalmers University of Technology. It covers all kind of research output: articles, dissertations, conference papers, reports etc. since 2004. research.chalmers.se is administrated and maintained by Chalmers Library

(article starts on next page)

Impact of Control Parameters on Angular Stability of Grid-Forming Converters Using Virtual-Admittance Based Control

Kavian Kamalinejad
Dept. of Electrical Engineering
Chalmers University of Technology
Göteborg, Sweden
kavian.kamalinejad@chalmers.se

Anant Narula
Dept. of Electrical Engineering
Chalmers University of Technology
Göteborg, Sweden
anant.narula@chalmers.se

Massimo Bongiorno
Dept. of Electrical Engineering
Chalmers University of Technology
Göteborg, Sweden
massimo.bongiorno@chalmers.se

Mebtu Beza
Dept. of Electrical Engineering
Chalmers University of Technology
Göteborg, Sweden
mebtu.beza@chalmers.se

Jan R. Svensson
Hitachi Energy Research
Hitachi Energy
Västerås, Sweden
jan.r.svensson@hitachienergy.com

***Abstract*—This paper investigates the impact of control parameters on the angular stability of grid-forming (GFM) converters using virtual-admittance-based control. The study focuses on a system operating under dynamic grid condition caused by the high penetration of renewable energy sources connected through power electronic converters. By drawing an analogy with a spring-mass-damper system to provide physical insight, it illustrates how the angles of individual masses, representing the converter and the grid, respond to a disturbance. A frequency-domain analysis identifies frequency regions where angle deviations are either amplified or attenuated as parameters are varied. The study examines how control settings, including active-power controller parameters, AC-voltage controller parameters, and virtual impedance, shape this dynamic response. The results highlight trade-offs in control design and offer practical guidance for tuning GFM converters to enhance angular stability under dynamic grid conditions. Finally, time-domain simulations validate the analytical findings.**

***Index Terms*—angular stability, grid-forming control, spring-mass-damper model, virtual-admittance.**

I. Introduction

While GFM converters have made significant advancements to overcome the challanges related to integration of renewable energy sources through voltage-source converters [1], similar to synchronous generators, they may encounter challenges related to transient stability. These challenges can be broadly categorized into two types: transient angle stability and transient voltage stability [2]. Angular stability, the focus of this paper, is vital for GFM converters to maintain the proper alignment of phase and frequency within the power grid. This stability ensures that the converters operate harmoniously with other grid components, preventing issues like phase divergence, which can lead to instability [3].

Many studies on angular stability have primarily focused on quasi-steady-state analyses, utilizing methods such as the power-angle curve and the equal-area criterion, which only account for mechanical dynamics [4], [5]. However, these approaches often neglect the influence of converter control parameters on dynamics, which can significantly impact the system's stability. As a result, they are not realistic for practical control system design, leading to an inaccurate assessment [3]. Alternatively, Lyapunov's direct method is a viable approach for transient stability assessment, but obtaining an appropriate Lyapunov function remains a significant challenge in practice [6]. Other numerical methods, such as time-domain simulations or phase portrait analysis, can be used to study angular stability but may require significant computational effort and still offer limited insight into how control parameters affect the dynamics [7]. In [8], the authors use phase portraits and also analyze the damping ratio, which influences overshoot, based on the effects of active and reactive power controller parameters. This gives a good insight on the impact of parameters on dynamic response; However, the derived damping ratio applies only to a specific, simplified controller configuration. These limitations underscore the need for more analytically tractable yet control-aware methods to evaluate and design stable grid-forming systems.

This paper aims to investigates how virtual admittance-based GFM (VA-GFM) control parameters influence the angular stability of a frequency-dynamic power grid, particularly in systems with high penetration of renewable energy sources. By drawing an analogy to a spring-mass-damper model, the study provides both physical intuition and analytical clarity, offering insight into the key parameters that may affect dynamic response and system stability. A small-signal model and frequency-domain analysis are developed to reveal how the dynamic behavior of VA-GFM converters can lead to growing angle differences between generating units, potentially resulting

in angular instability. This approach complements traditional quasi-steady-state analysis by showing that dynamic angle divergence can cause angle differences to exceed the critical thresholds defined by static criterion. This analysis is based on a small-signal model, valid near a fixed steady-state operating point. Since the control parameter variations explored in this paper do not or minimally affect this steady-state condition, the analysis remains valid and enhances traditional methods by incorporating dynamic system behavior. Furthermore, the proposed framework facilitates the analysis of multi-converter systems, enabling assessment of how disturbances propagate through the network and impact angular stability between different generating units.

II. Grid-forming control and system description

This section presents the system structure and introduces the VA-GFM control strategy used in this paper, with its detailed explanation provided in [9]. The system consists of a VSC connected to an AC grid through an inductive filter and a step-up transformer, as displayed in Fig. 1 (a). The VSC is controlled by VA-GFM control strategy, shown in Fig. 1(b). Moreover, the angular dynamics of the AC grid is represented by using the equation of motion, as illustrated in Fig. 1(c).

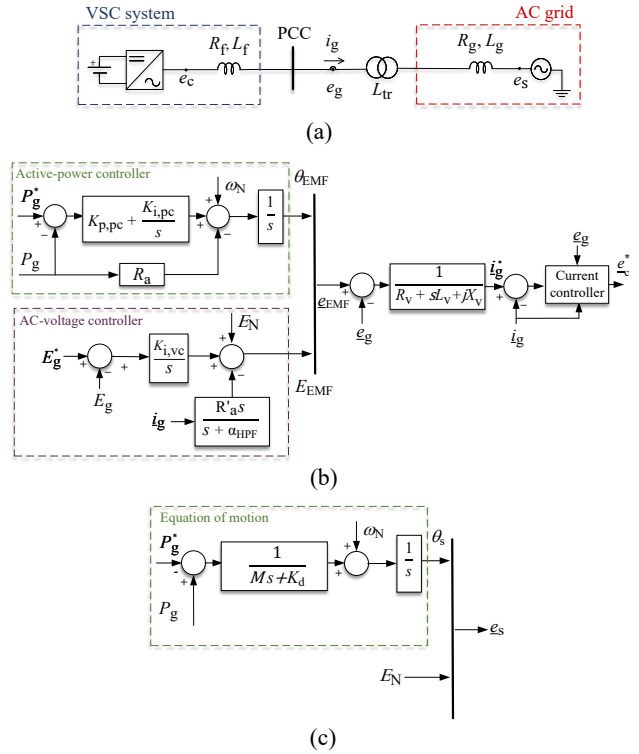


Fig. 1: (a) Structure of system. (b) Control structure of VA-GFM. (c) Model of dynamic AC grid.

In the active-power controller (APC) of VA-GFM, P_{g} and $P_{\mathrm{g}}^{\star}$ are the measured injected active power and its reference, respectively. $K_{\mathrm{p,pc}}$ and $K_{\mathrm{i,pc}}$ denote the proportional and integral gain of PI controller, respectively, and are tuned based on the desired bandwidth of APC (α_{pc}). In addition, (R_{a}) is an active damping term added to enhance the dynamic behavior of APC. The AC-voltage controller (AC-VC) is based on an integrator with the gain of $K_{\mathrm{i,vc}}$, which is used to regulate the magnitude of the voltage (E_{g}) at the point of common coupling (PCC) based on its reference ($E_{\mathrm{g}}^{\star}$). In the block diagram, E_{N} is the rated system voltage, and $R_{\mathrm{a}}^{'}$ is the gain of a transient damping controller implemented through a high-pass filter with the bandwidth of α_{HPF}. Moreover, L_{v} and R_{v} in Fig. 1(b) are the virtual inductance and resistance, respectively. The virtual admittance calculates the reference current $\underline{i}_{\mathrm{g}}^{\star}$, which is further sent to the current controller.

In addition, grid total inertia (M) is given by $\frac{2H}{\omega_{\mathrm{N}}}$ where H represents the inertia constant and is set to 5 second in this paper. Meanwhile, damping constant ($K_{\mathbf{d}}$) is defined as $2\zeta\sqrt{\frac{M}{L_{\mathbf{g}}}}$, where ζ denotes the damping ratio and is considered equal to 0.707 pu here.

The main circuit and controller parameters are listed in Table I. Note that the transformer is assumed to have a 1:1 turns ratio, with negligible leakage inductance.

TABLE I: circuit and control parameters (base case)

Parameter	Symbol	Unit
Nominal apparent power	S_{N}	100 MVA (1 pu)
Nominal RMS voltage	E_{N}	20 kV (1 pu)
Nominal frequency	f_{N}	50 Hz
Grid impedance (1/SCR)	L_{g}	1 pu
Grid inertia	M	0.0318 s^2
Damping constant	K_{d}	0.2523 s
Active power controller bandwidth	α_{pc}	5 Hz
Voltage controller bandwidth	α_{vc}	3 Hz
Active damping term	R_{a}	0.05 pu
Transient damping term	$R_{\mathrm{a}}^{'}$	0.1 pu
High-pass filter bandwidth	α_{HPF}	5 Hz
Filter resistance and inductance	R_{f}, L_{f}	0.015 pu, 0.15 pu
Virtual inductance	L_{v}	0.5 pu
Virtual resistance	R_{v}	0.25 pu

III. Analogy with the spring-mass-damper model

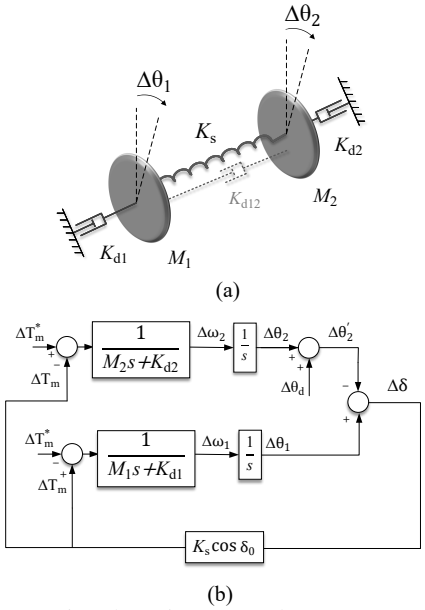
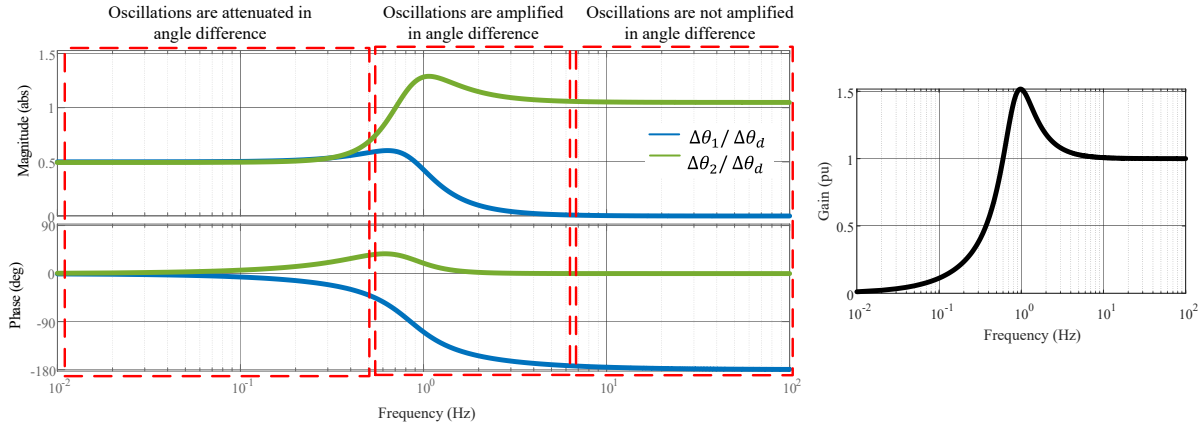


Fig. 2: (a) Torsional spring-mass-damper system. (b) Linearized block diagram of system.

$$\frac{\Delta\theta_1}{\Delta\theta_d} = \frac{K_{\mathrm{s}}^{'} M_2 s + K_{\mathrm{s}}^{'} K_{\mathrm{d2}}}{M_1 M_2 s^3 + (K_{\mathrm{d1}} M_2 + K_{\mathrm{d2}} M_1) s^2 + (K_{\mathrm{s}}^{'} M_1 + K_{\mathrm{d1}} K_{\mathrm{d2}} + K_{\mathrm{s}}^{'} M_2) s + K_{\mathrm{s}}^{'} K_{\mathrm{d1}} + K_{\mathrm{s}}^{'} K_{\mathrm{d2}}} \tag{1}$$

$$\frac{\Delta\theta_2}{\Delta\theta_d} = \frac{M_1 M_2 s^3 + (K_{\mathrm{d1}} M_2 + K_{\mathrm{d2}} M_1) s^2 + (K_{\mathrm{d1}} K_{\mathrm{d2}} + K_{\mathrm{s}}^{'} M_2) s + K_{\mathrm{s}}^{'} K_{\mathrm{d2}}}{M_1 M_2 s^3 + (K_{\mathrm{d1}} M_2 + K_{\mathrm{d2}} M_1) s^2 + (K_{\mathrm{s}}^{'} M_1 + K_{\mathrm{d1}} K_{\mathrm{d2}} + K_{\mathrm{s}}^{'} M_2) s + K_{\mathrm{s}}^{'} K_{\mathrm{d1}} + K_{\mathrm{s}}^{'} K_{\mathrm{d2}}} \tag{2}$$



(a) (b)

Fig. 3: (a) Bode plots from angle disturbance to angle of each mass. (b) Gain of angle difference between two masses with respect to angle disturbance.

In this section, a torsional spring-mass-damper model is studied, as shown in Fig. 2 (a). It consists of two masses (M_1 and M_2) connected together via a spring with a spring constant of K_{s}. The mass M_1 represents the grid-forming converter, while the other mass, M_2, represents the AC grid, and K_{s} denotes the inverse of inductance between the converter (or PCC) and the grid in the electrical system. Moreover, each mass has its own damper (K_{d1} and K_{d2}), which represents the damping contributed by the converter and the grid. Finally, in addition to the spring, a damper with a damping constant of K_{d12} can be considered between two masses, which is not studied in this paper.

The aim is to analyze how the angles of masses (θ_1 and θ_2) respond to an angular disturbance (θ_{d}) and how this behavior influences the angle difference between two masses (δ). The linearized block diagram of the system is illustrated in Fig. 2 (b), where the angular disturbance (θ_{d}) is applied to the second mass in this paper.

The transfer functions from the input disturbance, angle perturbation ($\Delta\theta_{\mathrm{d}}$), to resulting angle perturbation of two masses ($\Delta\theta_1$ and $\Delta\theta_2$) can be obtained as shown in (1) and (2), respectively, where $K_{\mathrm{s}}^{'}$, synchronizing torque coefficient, is equal to $K_{\mathrm{s}}\cos(\delta_0)$, with K_{s} denoting the maximum synchronizing torque coefficient and δ_0 representing the angle difference at the operating point.

To investigate how the angles of two masses, and the resulting angle difference between them respond to the input disturbance, frequency response of the transfer functions derived in (1) and (2) are presented with the parameter values of M=0.01, K_{d}= 0.05 for both masses, and K_{s}=1. These values serve as the base case for the remainder of this section. Additionally, the gain of the angle difference, derived from the phasor difference magnitude ($\left|\frac{\Delta\theta_1}{\Delta\theta_d} - \frac{\Delta\theta_2}{\Delta\theta_d}\right|$), is extracted from the plots in Fig. 3 (a) to illustrate the amplification or attenuation of disturbances in the angle difference across different frequency ranges in Fig. 3 (b). It can be observed from this figure that angle perturbation difference between two masses varies at different frequencies of input perturbation. Generally, Fig. 3 can be divided into three frequency ranges: at the low frequencies (0 to 0.5 Hz in this case), the resulting oscillations either have the same magnitude and phase, meaning the oscillations cancel out in the angle difference between the two masses, or they attenuate in the angle difference. This means that the system does not fall out of step. On the other hand, in the middle frequency range (approximately 0.5 to 5 Hz), oscillations phase starts to deviate from each other to 180 degrees. Therefore, oscillations are amplified in the angle difference and This increases the risk of losing angle stability. Finally, at higher frequency range (above 5 Hz), although phase shift is 180 degrees, magnitude of one bode plot is close to zero, meaning oscillations are not amplified in the angle difference.

To assess how the parameters of a spring-mass-damper model influence frequency responses and, in turn, the system's angular stability, different values of mass, damping coefficient, and spring constant are analyzed relative to the base case, as illustrated in Fig. 4. The results indicate that lighter masses prevent significant angle separation in low frequencies and also

reduce maximum amplification. Similarly, an increase in the damping coefficient results in lower amplification while there is a larger angle separation in low frequencies. Furthermore, increasing the spring constant keeps the angles tight together over a broader frequency range; However, this is accompanied by greater amplification in the middle frequency range

The advantage of having less angle separation at low frequencies comes from its high-pass filter-like behavior, which effectively suppresses low-frequency gains. This suppression ensures that the system returns to its operating point more quickly following a disturbance, such as a phase jump in the electrical system, thereby minimizing prolonged deviations. From a practical perspective, this feature is valuable because if stability is achievable after a disturbance, it reduces the need for large energy storage. By limiting prolonged active power exchange, the converter requires less buffered energy to maintain synchronism. Moreover, the presence of amplification caused by a second-order or higher-order response results in an overshoot when responding to a step input, which in the electrical system corresponds to a phase jump. Such an overshoot increases the risk of exceeding the critical angle difference, which can potentially destabilize the system, even if a stable operating point exists after the disturbance.

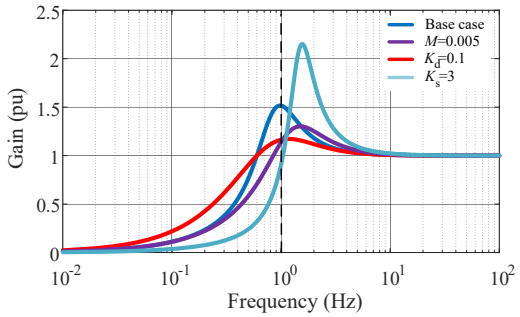


Fig. 4: Gain of the angle difference with different parameters.

To verify Fig. 4 and examine how the disturbance (angle perturbation) affects angular stability, time-domain simulation results from MATLAB/Simulink for the electrical equivalent of the spring-mass-damper model are shown in Fig 5. As demonstrated, a frequency of perturbation in the middle range (1 Hz) results in angle instability for the base case while lower and higher frequencies (0.5 Hz and 10 Hz, respectively) are not amplified in the angle difference. Moreover, it has been shown that with increasing spring constant and damping coefficient, angular stability can be gained for the applied angle perturbation (1 Hz) while decreasing mass values is beneficial for angular stability because in this frequency of perturbation gains are reduced compared to the base case. It is worth noting that this type of analysis is valid for disturbances modeled as sinusoidal perturbations, and is only applicable to small-signal angular stability where linearized frequency-response models are used. However, in the case of a phase jump, where all frequency components are excited, the key factor for angular stability becomes the maximum amplification across frequencies, as studied in the following section.

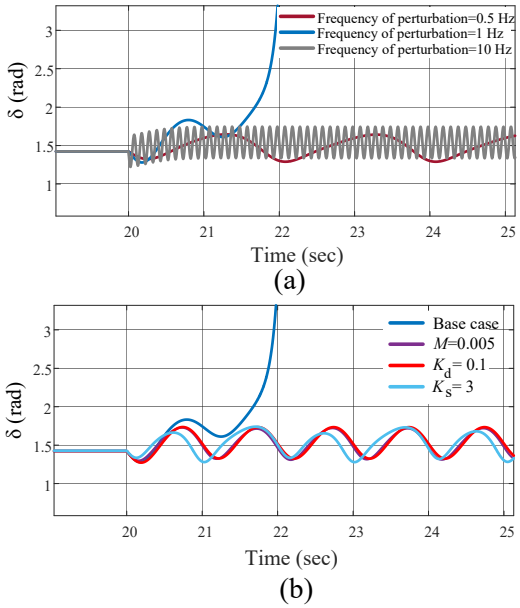


Fig. 5: Time-domain simulation results for angle difference between two masses resulting from angle perturbation. (a) different frequencies for angle perturbation. (b) impact of mass, spring constant, and damping coefficient on angle difference.

IV. Impact of Control Parameters on Angular Stability

The impact of control parameters in the VA-GFM strategy on the system's angular stability is investigated in this section. This is accomplished by employing the same approach described in Section III, where less angle separation in low frequencies and less maximum amplification is beneficial. Then, frequency-domain analysis is verified by time-domain simulation, where a 45 degree phase jump is applied to the grid.

To obtain the frequency response plots, the transfer functions $\frac{\Delta\theta_{EMF}}{\Delta\theta_d}$ and $\frac{\Delta\theta_s}{\Delta\theta_d}$ for the VA-GFM connected to the dynamic grid are derived based on the linearized model of the system.

$$\frac{\Delta\theta_s}{\Delta\theta_d} = [\mathbf{R}_1]_{2,1} \tag{3}$$

$$\frac{\Delta\theta_{EMF}}{\Delta\theta_d} = \frac{1}{s}\left[\mathbf{R}_1.\mathbf{R}_2\right]_{1,1}\mathbf{G}_{pc} \tag{4}$$

where

$$\begin{aligned}\mathbf{R}_1 = \Big(&\left(\mathbf{G}_{e\theta}\,\mathbf{G}_{\theta i}\,\mathbf{Z}_g^{-1} + \mathbf{G}_{e\theta}\,\mathbf{G}_{\theta e}\right)\mathbf{T}_g \\ &\cdot \left(\mathbf{G}_{tmc} + \mathbf{e}_{g0}\,\mathbf{Z}_g^{-1}\,\mathbf{T}_g + \mathbf{i}_{g0}\,\mathbf{T}_g\right)^{-1}\mathbf{e}_{g0}\,\mathbf{Z}_g^{-1}\,\mathbf{T}_s \\ &- \left(\mathbf{T}_s + \mathbf{G}_{e\theta}\,\mathbf{G}_{\theta i}\,\mathbf{Z}_g^{-1}\,\mathbf{T}_s\right)\Big)^{-1}\mathbf{G}_{e\theta}\end{aligned} \tag{5}$$

$$\mathbf{R}_2 = \left(\mathbf{I} + \left(\mathbf{e}_{g0}\,\mathbf{Z}_g^{-1}\,\mathbf{T}_g + \mathbf{i}_{g0}\,\mathbf{T}_g\right)\mathbf{G}_{tmc}^{-1}\right)^{-1}\mathbf{e}_{g0}\,\mathbf{Z}_g^{-1}\,\mathbf{T}_s \tag{6}$$

Most terms used in the expressions (5) and (6) are defined in [10], including $\mathbf{G}_{e\theta}$, $\mathbf{G}_{\theta i}$, $\mathbf{G}_{\theta e}$, $\mathbf{Z}_g$, $\mathbf{G}_{tmc}$, $\mathbf{G}_{pc}$, and the identity matrix $\mathbf{I}$.

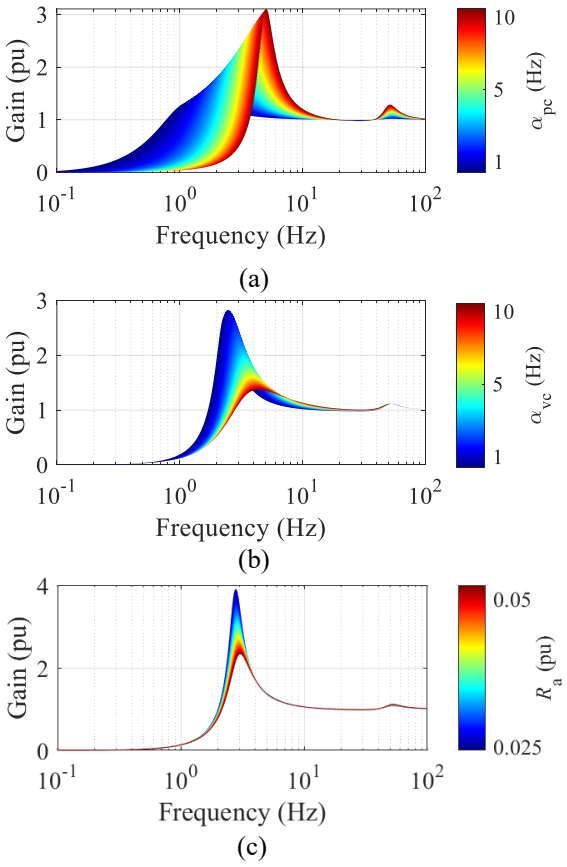


Fig. 6: Gain of angle difference with different values of APC and AC-VC parameters. (a) APC bandwidth ($\alpha_{\mathbf{pc}}$) (b) AC-VC bandwidth ($\alpha_{\mathbf{vc}}$) (c) active damping term (R_a)

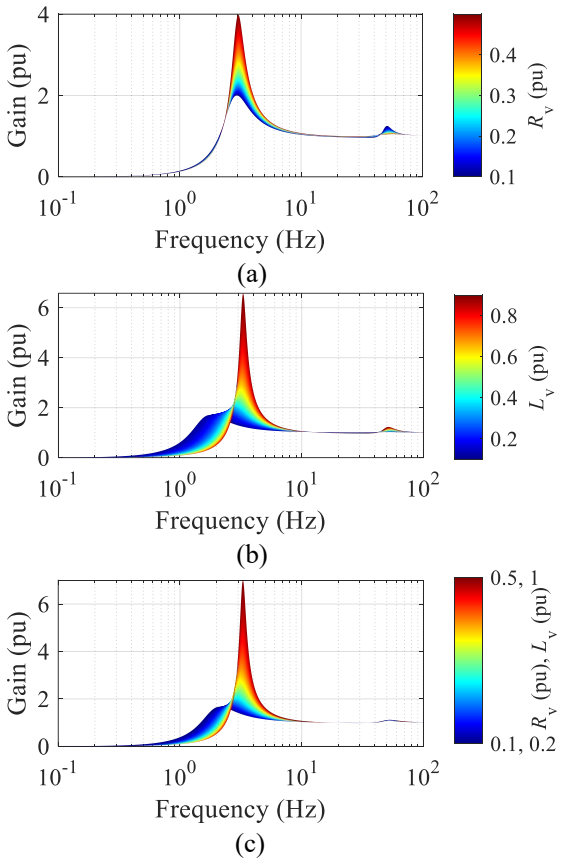


Fig. 7: Gain of angle difference with different values of virtual impedance. (a) virtual resistance ($R_{\mathbf{v}}$) (b) virtual inductance ($L_{\mathbf{v}}$) (c) same ratio of $L_{\mathbf{v}}$ and $R_{\mathbf{v}}$

The remaining symbols introduced here are as follows. The matrices $\mathbf{e}_{g0} = \begin{bmatrix} e_{gd0} & e_{gq0} \\ e_{gq0} & -e_{gd0} \end{bmatrix}$ and $\mathbf{i}_{g0} = \begin{bmatrix} i_{gd0} & i_{gq0} \\ -i_{gq0} & i_{gd0} \end{bmatrix}$ represent the steady-state voltage and current at grid connection point (PCC in this paper) in the synchronous rotating dq-frame, and correspond to the operating point around which the system is linearized. Moreover, the transformation matrices can be written as $\mathbf{T}_g = \begin{bmatrix} \cos(\theta_{g0}) & -\sin(\theta_{g0}) \\ \sin(\theta_{g0}) & \cos(\theta_{g0}) \end{bmatrix}$ and $\mathbf{T}_s = \begin{bmatrix} \cos(\theta_{s0}) & -\sin(\theta_{s0}) \\ \sin(\theta_{s0}) & \cos(\theta_{s0}) \end{bmatrix}$.

The gain of the angle difference between the GFM and the grid is plotted in Figs. 6 and 7 for various parameter values, considering a case where the GFM injects 0.8 pu of active power and the PCC voltage is regulated at 1 pu. As shown in Figs. 6 (a) and (b), the parameters α_{pc} and α_{vc} have opposite effects on amplification but a similar effect on convergence speed. Specifically, increasing the APC bandwidth (α_{pc}) accelerates convergence but worsens amplification, whereas increasing the AC-VC bandwidth (α_{vc}) enhances both convergence and damped response. This presents a trade-off in parameter design; high α_{pc} benefits convergence at the cost of increased amplification, while fast α_{vc} offers more favorable dynamic performance, although an overly fast AC-VC loop may conflict with the fundamental definition of a GFM converter. In addition, the effect of a small active damping term, which leads to higher amplification, is also evident in Fig. 6 (c). Furthermore, Figs. 7 (a) and (b) shows that higher values of virtual resistance and virtual inductance result in greater amplification. However, from the perspective of convergence speed, a higher virtual inductance contributes to faster dynamic response. Finally, Fig. 7 (c) demonstrates that even when the ratio between virtual inductance and resistance is kept constant, increasing their absolute values still leads to significantly higher amplification. Therefore, when designing virtual admittance, it is important to recognize that while it offers benefits in certain aspects, they do not necessarily contribute positively to angular stability.

Time-domain simulation results, shown in Fig. 8, support the frequency-domain analysis. Increasing a parameter that amplifies the system response relative to the base case leads to instability. Additionally, the simulations confirm the predicted convergence speed toward the post-disturbance operating point, further validating the analytical results. Since the

disturbance in this case is a phase jump, the post- and pre-disturbance operating points are identical. Even in the unstable case, the initial rate of approach to this point can still be observed and used to compare convergence speed.

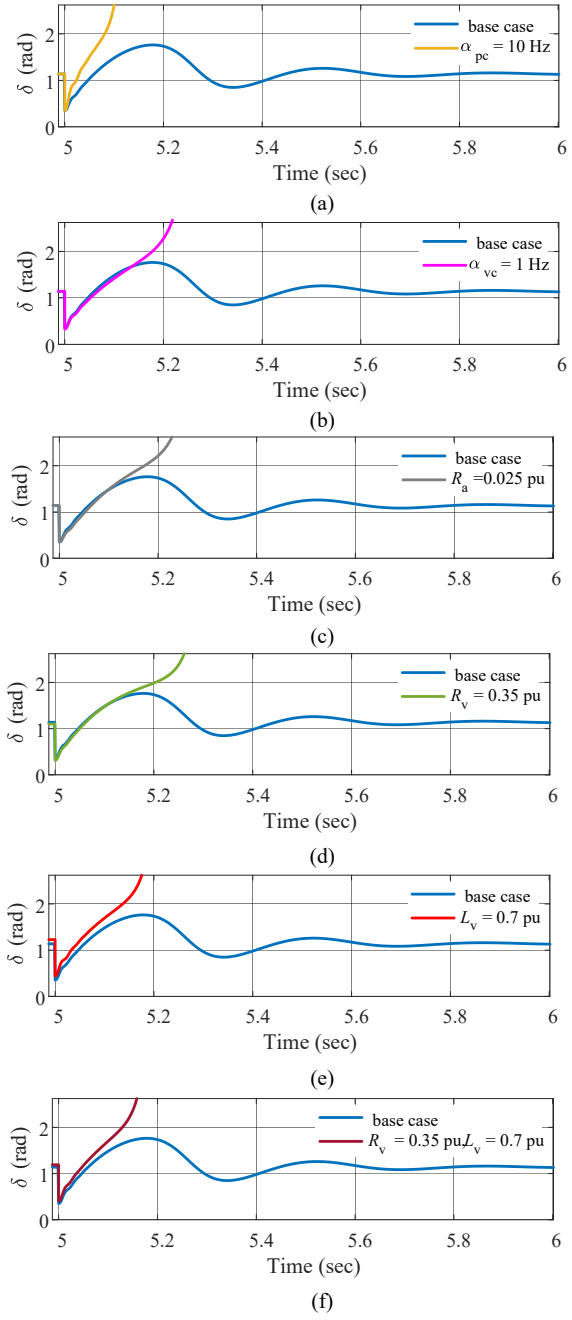


Fig. 8: Time-domain simulation results for a +45 degrees phase jump at t= 5 second with different values of control parameters compared with the base case. (a) higher value of $\alpha_{\mathbf{pc}}$ (b) lower value of $\alpha_{\mathbf{vc}}$ (c) lower value of $R_{\mathbf{a}}$ (d) higher value of $R_{\mathbf{v}}$ (e) higher value of $L_{\mathbf{v}}$ (f) same ratio but higher values of $R_{\mathbf{v}}$ and $L_{\mathbf{v}}$.

V. Conclusion

In this paper, the spring-mass-damper model has been used as an analogy to gain insights into the dynamic behavior of the GFM converter connected to the dynamic grid. The findings demonstrate that the angular stability of the converter is influenced by inertia of the grid, damping provided by the grid, and VA-GFM control parameters including virtual impedance and the parameters of APC and AC-VC. It has been shown that lower inertia and higher damping constant reduce the amplification of the disturbance in angle differences. However, while higher damping decreases convergence speed, lower inertia tends to accelerate it. Regarding GFM parameters, higher values of virtual inductance and resistance lead to greater amplification. Among these, virtual resistance has little effect on convergence speed, while increased virtual inductance accelerates the system dynamics. In terms of control bandwidth, an opposite trend is observed between the APC and AC-VC control loops in terms of amplification. Increasing the AC-VC bandwidth tends to reduce amplification and improve convergence, whereas increasing the APC bandwidth leads to higher amplification, despite improving the convergence speed Finally, reducing the active damping term has been shown to increase amplification.

References

[1] J. Matevosyan et al., "Grid-Forming Inverters: Are They the Key for High Renewable Penetration?," in *IEEE Power and Energy Magazine*, vol. 17, no. 6, pp. 89-98, Nov.-Dec. 2019, doi: 10.1109/MPE.2019.2933072.

[2] W. Si, W. Li, N. Tashakor and J. Fang, "Joint Transient Angle and Voltage Stability Analysis and Enhancement of Grid-Forming Converters," in *IEEE Transactions on Industrial Electronics*, doi: 10.1109/TIE.2024.3454767.

[3] X. Wang, M. G. Taul, H. Wu, Y. Liao, F. Blaabjerg and L. Harnefors, "Grid-Synchronization Stability of Converter-Based Resources—An Overview," in *IEEE Open Journal of Industry Applications*, vol. 1, pp. 115-134, 2020, doi: 10.1109/OJIA.2020.3020392.

[4] X. Xiong, C. Wu and F. Blaabjerg, "An Improved Synchronization Stability Method of Virtual Synchronous Generators Based on Frequency Feedforward on Reactive Power Control Loop," in *IEEE Transactions on Power Electronics*, vol. 36, no. 8, pp. 9136-9148, Aug. 2021, doi: 10.1109/TPEL.2021.3052350.

[5] K. Sun, W. Yao, J. Wen and L. Jiang, "A Two-Stage Simultaneous Control Scheme for the Transient Angle Stability of VSG Considering Current Limitation and Voltage Support," in *IIEEE Transactions on Power Systems*, vol. 37, no. 3, pp. 2137-2150, May 2022, doi: 10.1109/TPWRS.2021.3121474.

[6] Z. Shuai, C. Shen, X. Liu, Z. Li and Z. J. Shen, "Transient Angle Stability of Virtual Synchronous Generators Using Lyapunov's Direct Method," in *IEEE Transactions on Smart Grid*, vol. 10, no. 4, pp. 4648-4661, July 2019, doi: 10.1109/TSG.2018.2866122.

[7] Y. Liu, K. Sun, R. Yao and B. Wang, "Power System Time Domain Simulation Using a Differential Transformation Method," in *IEEE Transactions on Power Systems*, vol. 34, no. 5, pp. 3739-3748, Sept. 2019, doi: 10.1109/TPWRS.2019.2901654.

[8] D. Pan, X. Wang, F. Liu and R. Shi, "Transient Stability of Voltage-Source Converters With Grid-Forming Control: A Design-Oriented Study," in *IEEE Journal of Emerging and Selected Topics in Power Electronics*, vol. 8, no. 2, pp. 1019-1033, June 2020, doi: 10.1109/JESTPE.2019.2946310.

[9] K. Kamalinejad, A. Narula, M. Bongiorno, M. Beza and J. R. Svensson, "Investigation of Control Parameters' Impact on Damping Property of Grid-Forming Converters," 2024 *IEEE Energy Conversion Congress and Exposition (ECCE)*, Phoenix, AZ, USA, 2024, pp. 686-693, doi: 10.1109/ECCE55643.2024.10860863.

[10] A. Narula, P. Imgart, M. Bongiorno, P. Mattavelli, M. Beza and J. R. Svensson, "Power-Response Matrix-Based Modeling of Converter Systems for Small-Signal Analysis," 2024 *IEEE Energy Conversion Congress and Exposition (ECCE)*, Phoenix, AZ, USA, 2024, pp. 4724-4731, doi: 10.1109/ECCE55643.2024.10860906.